Design of Semi-Active Vibration Control Device for Commercial Pump Systems

O.S. Hermansen, M.A. Jensen, S.H. Søndergaard, R. Sørensen, N.B. Winther

Department of Materials and Production, Aalborg University
Fibigerstræde 16, DK-9220 Aalborg East, Denmark
Email: {oherma18,majens18,ssand18,rsa18,nwith18}@student.aau.dk,
Web page: http://www.mechman.mp.aau.dk/

Abstract

This project is made in collaboration with Grundfos to reduce vibration issues of their pump systems due to resonance. A Smart Device which adaptively can change the eigenfrequency of the system is designed.

The Smart Device works as an added support which provides stiffness to the system using a frictional contact. Two different approaches are used for its optimisation in order to compare the methods and benefit from the advantages of each method. Explicit optimisation is conducted using the Monte Carlo method to determine a starting guess for a gradient-based approach which provides the optimum. Separately, implicit optimisation using ANSYS is conducted to access the problem using a finite element approach. The two obtained designs are compared and a final design is made utilising elements from each method.

To validate whether the obtained design can increase the eigenfrequencies of the system, modal- and harmonic analysis is conducted in ANSYS for the Smart Device in its activated and deactivated state. The Smart Device is found to increase the eigenfrequencies in the desired frequency range. The location of the device is found to have a significant influence on the ability to increase eigenfrequencies. For this reason, an application is developed to determine the optimum location of the Smart Device.

Keywords: Mechanical Vibrations, Resonance, Modal & Harmonic Analysis, Semi-Active Vibration Control, Design & Optimisation

Disclaimer: Due to confidentiality with Grundfos some information is withheld.

1. Introduction

This article investigates the possibility of designing a semi-active vibration control device (Smart Device) that can prohibit the undesirable effects of resonance. It will address the following topics in the associated sections:

- Initial investigation in Section 2 establishes a baseline for the design case along with presentation of concept and the chosen material.
- Requirements in Section 3 is a selection of the fundamental design requirements based on the initial investigation.
- Synthesis of the Smart Device in Sections 4 and 5 handles the design phase with two explicit methods: Monte Carlo and gradient-based optimisation using MATLAB and one implicit method using ANSYS to optimise the dimensions of the Smart Device.
- Validation in Section 6 investigates the fulfillment of the requirements by analysing the deactivated and activated state of the Smart Device in a pump system. The validation handles an eigenfrequency and frequency response analysis.
- Location of the Smart Device in Section 7 describes the development of an application to evaluate the optimal location for the Smart Device on a pump system based on the mode shapes of the system.

2. Initial Investigation

Based on initial tests performed by Grundfos, desirable results are observed by changing the stiffness of a pump system when operating close to its resonance frequency. Due to the shift in resonance frequency obtained by the changed stiffness, the pump system no longer exhibits increased amplitude as the resonance peak has been moved from the frequency of excitation.

Due to requirements from Grundfos, the Smart Device must be placed between the pump system and foundation. The positioning of the Smart Device is critical in its ability to change its properties. As such, proper positioning must also be found.

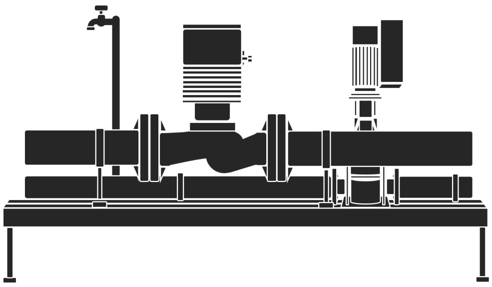

Fig. 1 Skid pump system investigated.

The pump skid systems considered in this article is presented in Fig. 1. This type of pump system are used for commercial applications where a large flow is needed. These systems consist of a mounting skid where an assembly of pumps and monitoring equipment are attached. These systems can be customised to meet consumer needs which means that the size can vary considerably. These systems are typically either bolted to the floor or resting on supports.

To implement the Smart Device in a pump system it must be attached separately from the load-bearing supports in the system. The dead weight of the pump system must be supported at all times through the regular load-bearing supports as the Smart Device in a deactivated state is not able to transfer any load.

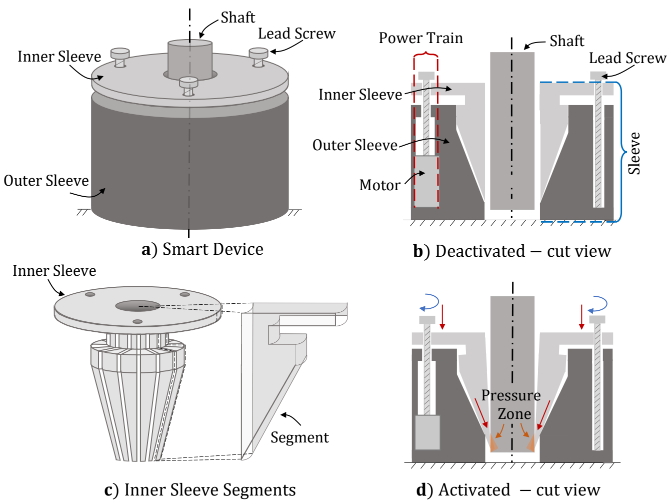

Fig. 2 Smart Device concept.

Conceptually, the Smart Device is created through a brain storming process. Fig. 2 illustrates the concept. In this concept, the outer sleeve and power train are fixed to the foundation. The shaft is attached to the pump system and can freely vibrate in the deactivated state. When activated, the lead screws bring the inner sleeve down into the outer sleeve resulting in clamping of the shaft. The clamping movement initiates a deflection of the inner sleeve establishing a friction contact with the shaft that restricts vibration. To enable easier deflection the lower part of the inner sleeve is sliced as shown in Figure 2. The element formed from the sliced lines is referred to as a segment. The inner sleeve is divided into 12 segments about the centre of the shaft.

In the initial assessment of performance it is found that a high yield strength is needed. In this regard the material chosen for the inner sleeve is quenched and tempered AISI 4340 steel with a yield strength of $1300\,\mathrm{MPa}$. The material is presented here as the value is needed for the synthesis in Sections 4 and 5.

3. Smart Device Requirements

From conversation with Grundfos along with the previously presented analyses of the pump systems, a set of requirements for the Smart Device are formulated. The design of the device is based on the semi-active vibration control principle and aims to fulfill the following requirements:

1) Change stiffness of pump system at least 21%.
2) Change eigenfrequency for pump system in the range $25\,\mathrm{Hz}$ to $100\,\mathrm{Hz}$.
3) Energy consumption of device lower than 10% of the pump.
4) Response time less than $30\,\mathrm{s}$.
5) Function on all skid pump systems.
6) Maximum height of $85\,\mathrm{mm}$.
7) Minimum allowable vertical movement of $1\,\mathrm{mm}$ for the system in the deactivated state.
8) Withstand vertical force of at least $700\,\mathrm{N}$ in the device.

4. Explicit Synthesis of Smart Device

Synthesis is performed to determine the optimum dimensions of the Smart Device presented in Section 2. The synthesis is divided into two parts, the first part is based on explicit equations and the second is based on implicit computations from ANSYS. The optimisation scheme for the explicit part is performed both with the Monte Carlo method and a gradient-based method. The intention of using multiple different optimisation methods is to compare and choose the optimal design dimensions based on different approaches to the problem. The following section will investigate the explicit optimisation scheme.

The aim of the design is the ability to use contact properties to clamp the shaft to the sleeve and increase the overall stiffness of the pump system. To ensure this clamping, the frictional force F_a between the shaft and inner sleeve is of interest. The object function is formulated based on the friction formulation given in Eq. (1), where F_{shaft} is the normal force between the shaft and inner sleeve, μ is the coefficient of friction between the two surfaces, and n is the number of segments.

$$F_a = n\, F_{shaft}\, \mu \tag{1}$$

The following sections investigate the relevant constraints to be used in Monte Carlo and gradient-based optimisation:

- The geometrical relations is established in Section 4.1.
- Force and moment equilibrium is formulated in Section 4.2.
- The compatibility between the force induced displacements and the total displacement is ensured in Section 4.3.
- Stress evaluation in the contact point, lead screw, and bending of inner sleeve is derived in Section 4.4.

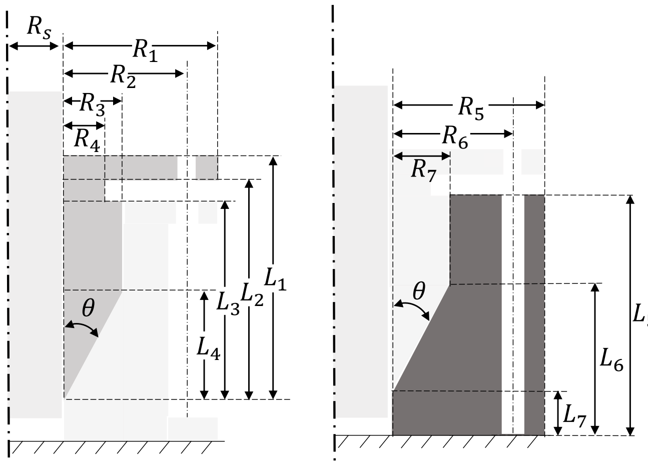

Fig. 3 Geometrical dimensions of Smart Device.

4.1 Geometrical Considerations

It is important to ensure that all geometric sizes are considered for the design of the device to be feasible. These geometric constraints ensure geometric relations of the structure and alignment with the power train. All dimensions in Fig. 3 are specified as geometric design variables, some of which are interdependent, resulting in a set of equality- and inequality constraints.

4.2 Equilibrium Conditions

Both force- and moment equilibrium are ensured based on Fig. 4 resulting in Eqs. (2) to (4), where the deformation angle φ is assumed to be negligible.

$$\begin{aligned}\sum F_x = F_{shaft} - F_{sleeve}\cos(\theta) \\ + \mu\, F_{sleeve}\sin(\theta) - F_{screw} = 0\end{aligned} \tag{2}$$

$$\begin{aligned}\sum F_y = \mu\, F_{shaft} + \mu\, F_{sleeve}\cos(\theta) \\ + F_{sleeve}\sin(\theta) - F_{PT} = 0\end{aligned} \tag{3}$$

$$\begin{aligned}\sum M_{point} = -F_{PT}\, R_2 + F_{screw}\,\frac{L_1 + L_2}{2} \\ + F_{sleeve}\,\frac{d}{\cos(\theta)} - M = 0\end{aligned} \tag{4}$$

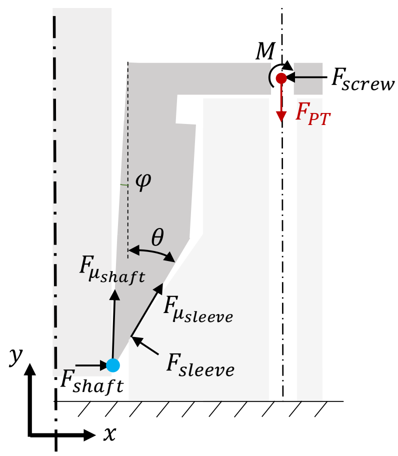

Fig. 4 Forces- and moments acting on inner sleeve.

The three equilibrium equations provide the following five unknowns: F_{sleeve}, F_{shaft}, F_{PT}, F_{screw}, and M. Since the system is under-determined further investigation is needed.

4.3 Compatibility

The displacements are investigated to ensure compatibility and thereby giving five equations with five unknowns. The undeformed and assumed deformed geometries are shown in Fig. 5. A torque T is applied resulting in a vertical force F_{PT} in the lead screw, leading to a vertical- and transverse displacement, d and Δ respectively. Following the applied load, compatibility of the inner sleeve and shaft must be ensured. Again, the deformation angle φ is negligible, thus the vertical part of the inner sleeve only translates. Hence it is assumed that the entire inner sleeve moves along the contact surface between the inner- and outer sleeve as illustrated in Fig. 5. The transverse displacement is given by Eq. (5) which relates the easier controllable displacement d.

$$\Delta = \tan(\theta)\, d \tag{5}$$

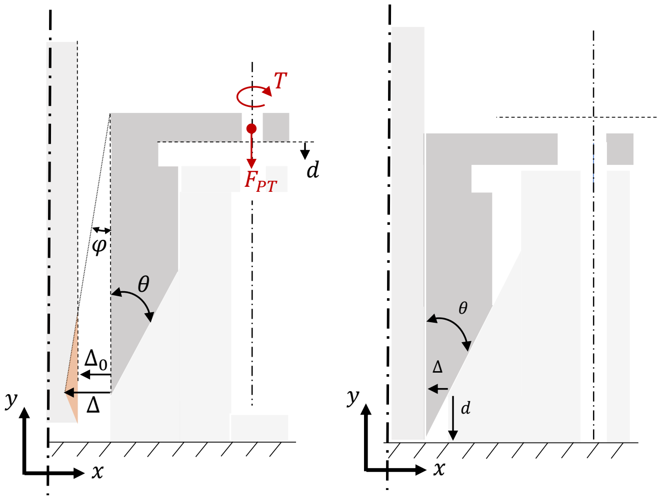

Fig. 5 Geometric behaviour and assumed behaviour.

Assuming the vertical part of the inner sleeve can be considered as a cantilever beam, three forces contribute to the deformation Δ: F_{shaft}, F_{sleeve}, and $F_{\mu_{sleeve}}$. Each force contribution to the deflection is found from a Bernoulli-Euler cantilever beam model. By using the principle of superposition, a relation between F_{sleeve} and F_{shaft} is derived in Eq. (6).

$$F_{sleeve} = \frac{6\, E\, I_v\, \Delta + 2\, F_{shaft}\, L_2^3}{(\cos(\theta) - \mu\, \sin(\theta))\, (L_2 - d)^2\, (2L_2 + d)} \tag{6}$$

To formulate F_{shaft} independent from other forces the relation between force and displacement is established using point-to-point contact. Hertzian contact theory for a point-to-point contact is defined as Eq. (7) [1].

$$F_{shaft} = \sqrt{\left(\frac{\delta_{shaft}}{0.775}\right)^3 \frac{1}{\left(\frac{1}{E_s} + \frac{1}{E_h}\right)^2 \left(\frac{1}{R_s} - \frac{1}{R_s + \Delta_0}\right)}} \tag{7}$$

Where δ_{shaft} is the difference between the displacement Δ and the initial gap $\Delta_0 = 0.5\,\mathrm{mm}$.

The five unknowns: F_{sleeve}, F_{shaft}, F_{PT}, F_{screw}, and M can now be found from the equilibrium equation in Eqs. (2) to (4) along with the compatibility equations in Eqs. (6) and (7).

4.4 Stress Evaluation

To ensure the synthesised design does not result in max stresses which exceeds the yield strength of the chosen material the stress aspect is investigated. Four critical areas on the inner sleeve are investigated w.r.t. stresses: contact stresses between the inner sleeve and shaft, lead screw stresses, and normal and bending stresses in the inner sleeve.

Shaft Contact Stresses

As mentioned, the contact stresses are estimated with Hertzian stresses, and as such, are given by Eqs. (8) and (9) where a_{shaft} is the radius of the contact path [1].

$$\sigma_{shaft,x} = -\frac{3}{2} \frac{F_{shaft}}{\pi a_{shaft}^2} \tag{8}$$

$$\sigma_{shaft,y} = \sigma_{shaft,z} = -\frac{3}{2} \frac{F_{shaft}}{\pi a_{shaft}^2} \left(\frac{1 + 2\,\nu}{2}\right) \tag{9}$$

Lead Screw Stresses

The lead screw stresses are governed by the applied torque T, the resulting normal load F_{PT}, the reaction force F_{screw} and moment M. The normal stresses are due to the normal axial load and the bending contribution as shown in Eq. (10), where d_p is the pitch diameter and d_r is the minor diameter of the lead screw [2].

$$\sigma_{n_{screw}} = \frac{16 F_{PT}}{\pi\, (d_p + d_r)^2} + \frac{32 |F_{screw}\, (L_2 + L_7) - M|}{d_r^3\, \pi} \tag{10}$$

The shear stress in the lead screw threads is given by Eq. (11), where the shear contribution from F_{screw} is neglected. The applied torque contributes to shear stress given by Eq. (12) [2].

$$\tau_{s_{screw}} = \frac{F_{PT}}{\pi\, d_r\, w_i\, l} \quad (11) \qquad \tau_{t_{screw}} = \frac{16\, T}{\pi\, d_r^3} \quad (12)$$

Inner Sleeve Normal- and Bending Stresses

The inner sleeve is assumed to be comprised of a horizontal- and vertical Bernoulli-Euler beam as shown in Fig. 6. The normal- and bending stresses of these beams are expressed in the following. The shear stresses are assumed to be negligible small compared to the normal- and bending stresses.

The maximum bending stress in the horizontal beam is given by Eq. (13). F_{screw} contributes to normal stress

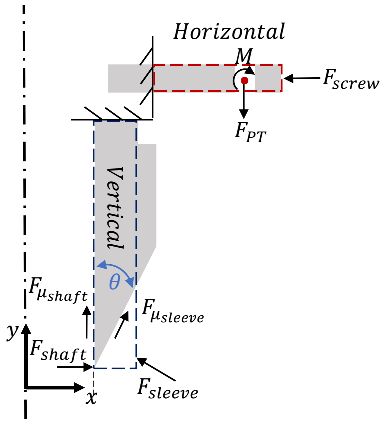

Fig. 6 Dividing inner sleeve into horizontal (red) and vertical (blue) cantilever beams.

in the horizontal beam, given by Eq. (14) where I_h is the second moment of area.

$$\sigma_{h_b} = \frac{\left(F_{PT}\left(R_2 - R_4\right) + M\right)\left(L_1 - L_2\right)}{2I_h} \tag{13}$$

$$\sigma_{h_n} = \frac{F_{screw}}{\left(R_s + \Delta_0 + R_1\right)\sin\left(\frac{\phi}{2}\right)\left(L_1 - L_2\right)} \tag{14}$$

Similarly, the normal stress in the vertical beam due to the bending and normal stresses are determined as shown in Eqs. (15) and (16).

$$\sigma_{v_b} = \frac{R_4}{2I_v}[F_{shaft}\,L_2 - F_{sleeve}\,(L_2\,\cos(\theta) - d\,\cos^{-1}(\theta)) + F_{\mu sleeve}\,L_2\,\sin(\theta)] \tag{15}$$

$$\sigma_{v_n} = \frac{F_{\mu shaft} + F_{sleeve}\,\sin(\theta) + F_{\mu sleeve}\cos(\theta)}{\frac{\phi}{2}\left(\left(R_4 + R_s + \Delta_0\right)^2 - \left(R_s + \Delta_0\right)^2\right)} \tag{16}$$

This provides the relevant constraints to be used in a Monte Carlo and a gradient-based optimisation scheme. Section 4.1 provides design variables where some are interdependent resulting in equality- and inequality constrains. Sections 4.2 and 4.3 gives equality constrains based on equilibrium and compatibility, and the stress evaluation in Section 4.4 provides inequality constrains.

4.5 Synthesis Practice

As mentioned, the Monte Carlo- and gradient-based method are used to perform the optimisation of the explicit equations.

Monte Carlo Method

The Monte Carlo method is inefficient as a large number of calculations with randomly chosen numbers are performed to estimate the global optimum. The method is robust for finding global optimum in contrast to gradient-based methods which might converge to local optima. As the method uses randomly generated values it is unlikely that all equality and inequality constraints will be satisfied to obtain a feasible solution. For this reason, some design variables are expressed through equality constraints and are not included as variables for random generation. The remaining design variables are presented with limit values in Tab. I.

The Monte Carlo method is performed in MATLAB using the *rand* function that allows for a uniform randomly distributed number of the design variables.

D.V.	R_s	θ [°]	Δ	R_3	R_4	L_1	L_2	L_3	L_5
lb	5	0	0.5	3	3	30	25	25	25
ub	20	30	0.51	30	20	60	50	50	50

Tab. I Design variables (D.V), the upper (ub) and lower bounds (lb). Units in [mm] unless specified otherwise.

Gradient-Based Method

The gradient-based optimisation is performed using the MATLAB function *fmincon* as shown in Eq. (17). This method allows for both linear and non-linear constraints. However, the equality constraints are used identically to the Monte Carlo method. The start guesses for the gradient-based method are obtained from the Monte Carlo optimisation results.

$$\text{minimize } f(x) \text{ such that } \begin{cases} c \leq 0 \\ c_{eq} = 0 \\ A\,x \leq b \\ A_{eq}\,x = b_{eq} \\ lb \leq x \leq ub \end{cases} \tag{17}$$

Performing the optimisation with the Monte Carlo method and the *fmincon* solver in MATLAB gives the results in Tab. II.

Method	Obj [kN]	R_s [mm]	θ [°]	Δ [mm]	R_3 [mm]	R_4 [mm]	L_1 [mm]	L_2 [mm]	L_3 [mm]	L_5 [mm]
M.C.	1.38	11.5	10.05	0.505	3.84	3.42	46.4	42.7	28.07	32.06
fmincon	1.65	12.5	9.11	0.506	3.05	3.05	47	44.6	28	25

Tab. II Results from optimisation using Monte Carlo and *fmincon* solver.

From the table, it is seen that the *fmincon* solver has converged to a 16% better optimum than the Monte Carlo method.

5. Implicit Synthesis of Smart Device

Separate from the explicit synthesis, a finite element model is used to generate an implicit numerical solution.

The geometry is similar to the model used in the explicit optimisation regarding general shape and functionality. However, only two design variables are included to reduce simulation time. The contact angle of the inner- and outer sleeve are varied in the interval 12° to 15° and 12° to 17° respectively, and the remaining geometry is defined to follow these changes. The angles are shown in Fig. 7. Fillets have iteratively been added to the model to reduce high stresses at specific locations. To reduce the computational cost of the simulations a quarter model is investigated with symmetry boundary conditions. A load of 1500 N is applied at the lead screw location and the resulting reaction force in the shaft fixation is found as the objective for the optimisation.

Due to asymmetry in the mesh, the initiation of contact at each segment varies. This causes undesirable rotation of the inner sleeve due to the established friction to the outer sleeve. This is solved using a shared angle at the bottom of each segment where the initial contact will occur.

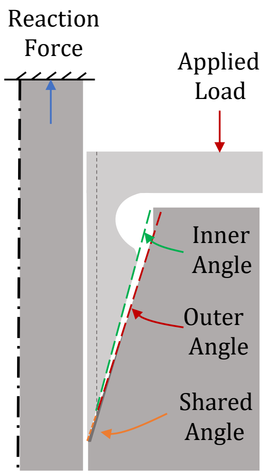

Fig. 7 Quarter model with boundary conditions.

Simulations are conducted for various combinations of sleeve angles and the results in terms of frictional reaction force and stresses in the geometry are obtained. Fig. 8 visualises the reaction force and maximum equivalent stress for the inner sleeve which is found to be the critical part. Each colour indicates a fixed value of the inner sleeve angle where the value of the outer sleeve angle is varied. The greatest outer sleeve angle results in the lowest reaction force for each colour. The optimum is found based on the graphical representation.

The maximum allowable stress dictated by the material chosen in Section 1 and minimum required reaction force from requirement 8 in Section 3 are shown by the vertical and horizontal black lines where the infeasible domain is marked with grey. From the figure, it is seen that the optimum reaction force is 281 N resulting in an equivalent stress of 1244 MPa. This correspond to 1.12 kN of reaction force for a full model. This result is obtained using an inner angle of 12.5° and an outer angle of 14°.

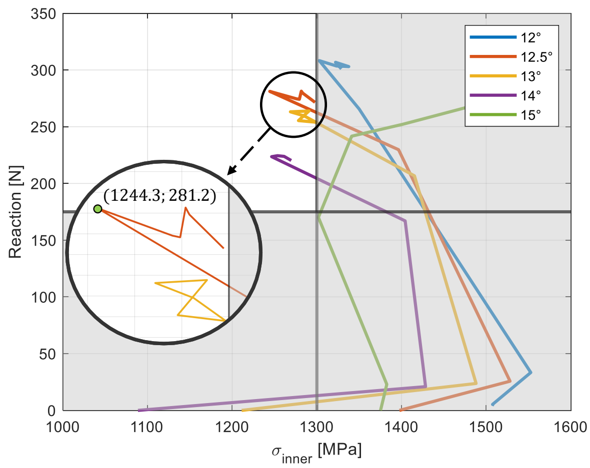

Fig. 8 Graphical representation of reaction force and stress in inner sleeve for various sleeve angles.

5.1 Final Design of Smart Device

To determine the final design from the two independent optimised solutions a comparison of the performance of the designs are conducted. A static structural analysis is conducted iteratively in ANSYS to result in the minimum required reaction force of 700 N by varying the applied load. Equivalent stresses for the shaft, inner- and outer sleeves are compared along with the necessary lead screw force to determine which design has the lowest stress and -torque requirement. Tab. III shows this comparison.

Parameters	Explicit	Implicit	Final
Reaction force [N]	707	709	717
Max. inner stress [MPa]	1170	1200	857
Max. outer stress [MPa]	25.0	289	281
Max. shaft stress [MPa]	23.4	58.1	36.2
Lead screw force [N]	820	1220	850

Tab. III Parameters compared between the explicit and implicit design schemes.

Even though the ANSYS optimised geometry includes stress reducing fillets and other geometrical features which have not been taken into consideration in the explicit design, it is evident from the table that the design from the explicit approach results in lower stresses and less required torque from the motor. For this reason a final design based on the explicit design with added stress reducing fillets is selected.

Having the final dimensions for the shaft and sleeves with the required motor torque, a power train is designed to achieve a fully functional Smart Device. The final design is shown in Fig. 9. An exploded view is shown in Fig. 15 on page 10.

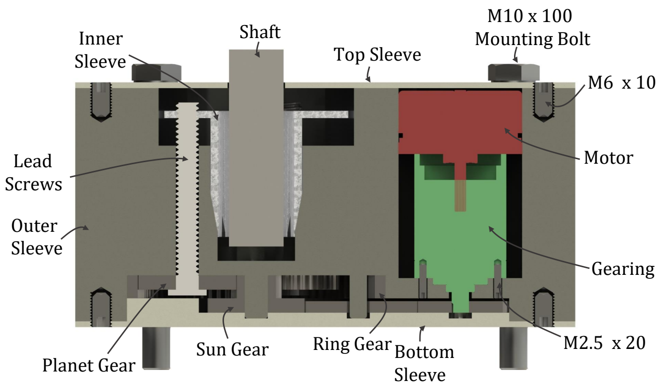

Fig. 9 Section view of final design.

6. Validation

Validation of the Smart Device is assessed by numerical modelling of the ability to change the eigenfrequencies and its frequency response function through ANSYS simulations.

6.1 Defeaturing of Pump Systems

Grundfos has provided CAD models for the validation. However, these models are too detailed as shown in Fig. 10. This causes issues both when meshing the geometries but also in terms of solution time when performing an analysis.

Removing the smaller details is a reasonable approach as the interest is the global mode shapes. For global mode shapes the entire structure vibrates whereas for local mode shapes only parts of the structure are excited. The global mode shapes are governed by the general shape, mass, and stiffness of the pump and skid. This means that removing details in this way has a negligible effect on the global mode shapes.

For both models, only the base platform, pipes, pump- and motor housings are retained. To account for the

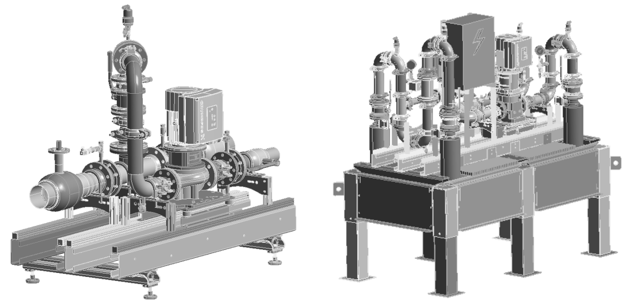

Fig. 10 Pump systems supplied by Grundfos. **(L)** Skid pump system I. **(R)** Skid pump system II.

lost mass, the density of the remaining parts are adjusted accordingly. This ensures that the overall global response of the simplified system is similar to the original system. The simplified geometries are shown in Fig. 11.

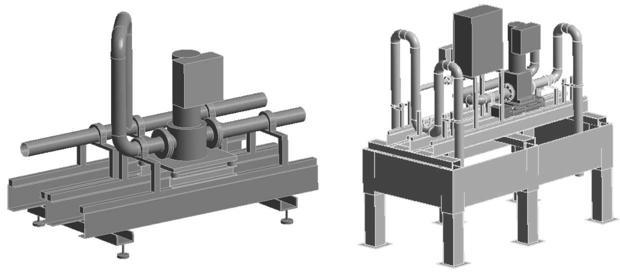

Fig. 11 Simplified pump systems. **(L)** Skid pump system I. **(R)** Skid pump system II.

When performing free vibration analyses on the simplified geometries it should be noted that the eigenfrequencies will differ from the true eigenfrequencies. However, as the phenomenon of moving the eigenfrequency can still be studied even with slight inaccurate values, this problem is not paramount. For the Smart Device to function as intended the mode shapes are of greater importance. The mode shapes of the general pump structures are less prone to differ even with a coarse geometry and discretisation.

6.2 Modal Analysis

To validate that the Smart Device can alter the eigenfrequencies of the pump systems, modal analyses are conducted for both the simplified CAD models. Two versions of each model are created, one without the Smart Device referred to as deactivated and one where the Smart Device is added as non-load-bearing support below the mounting plate, this state is referred to as activated.

As shown in Tab. IV the Smart Device can change the eigenfrequency of the system I by at least 131% within the operational frequency of the pump when activated, validating that it can provide the needed stiffness.

	ω_1	ω_2	ω_3
Deactivated	40.3	40.4	122
Activated	93.1	109	199
Rel. increase	131%	170%	63%

Tab. IV Change in eigenfrequency of Smart Device on skid system I. Frequencies in [Hz].

For the skid pump system II the first five mode shapes are global modes. Upon attaching the Smart Device to the system a shift from global to local modes is observed and only a small change in eigenfrequency is recorded for four out of five eigenfrequencies as shown Tab. V. This is likely due to the stiffer support legs than that of system I. For this reason, a different approach for vibration control for skid pump system II must be taken.

	ω_1	ω_2	ω_3	ω_4	ω_5
Deactivated	37.3	44.2	57.8	67.0	93.8
Activated	39.0	46.3	59.9	91.7	98.5
Rel. increase	5%	5%	4%	37%	5%

Tab. V Change in eigenfrequency of Smart Device on skid system II. Frequencies in [Hz].

6.3 Harmonic Analysis

Validation of the behaviour of the skid system I, with the Smart Device both activated and deactivated is conducted using a harmonic analysis. The harmonic analysis solves the equations of motion in the frequency domain when a harmonic force is applied. In this case a rotating force with unbalance of $1250\,\mathrm{g\,mm}$ in the rotor is used as the forcing load.

The behaviour of the pump system is shown in Fig. 12 where an increase in eigenfrequencies in the operating frequency spectrum is observed.

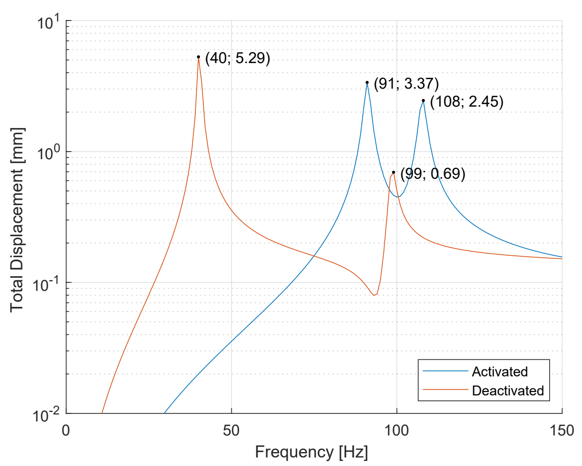

Fig. 12 Frequency response of total displacement of skid pump system I. (Damping $c = 0.02$)

Based on the validation analysis the Smart Device demonstrates an acceptable ability to change stiffness, thereby eigenfrequency and frequency response characteristics. As seen in Fig. 12 the second eigenfrequency of the deactivated state is lower than the corresponding eigenfrequency obtained from the modal analysis from Tab. V. This indicates a reduction in stiffness of this mode due to the applied rotating force. It is speculated that parametric excitation causes this phenomenon however it will not be investigated further.

It is seen from the figure that having an operating frequency of $90\,\mathrm{Hz}$ to $100\,\mathrm{Hz}$ can lead to resonance issues in the analysed configuration of device location as peaks are observed both in an activated- and deactivated state. This issue can be solved by relocating the Smart Device or adding multiple devices to the pump system allowing for better control over the frequencies at which resonance occurs. Based on this observation it is beneficial to determine the optimum device location from the operating frequency of the pump system. This is further investigated in the forthcoming section.

7. Application for Optimum Smart Device Location

The location of the base supports have a significant influence on the eigenfrequencies and mode shapes of the geometry. The Smart Device is intended to be placed where the mode shape displacements are at a maximum to have the greatest effect on the eigenfrequencies. Identical pump systems can not be expected as individual installations vary with the consumer's needs. As a result, the optimum location for the Smart Device depends on the configuration of the pump setup. An application is developed in MATLAB App Designer, to allow a service technician to install the Smart Device in the best possible location with limited knowledge of vibrations. The app is limited to simple setups, where the entire base of the skid is assumed to be a vibrating beam in bending with one or several point masses to represent the pumps on the skid.

7.1 Mode Shapes of Pump Systems

To find the optimum location for the Smart Device, the eigenfrequencies and mode shapes are determined using Rayleigh-Ritz's method. The stiffness a_{ij} and mass D_{ij} matrices are established using Eqs. (18) and (19). These are established by approximating the mode shape ϕ_i. In these equations k_n and m_n is the n'th spring and point mass located at x_{nk} and x_{nm} and is visualised in Fig. 13.

$$a_{ij} = \int_0^L EI\,\phi_i''\,\phi_j''\mathrm{d}x + \sum_{n=1}^{N_k} k_n\,\phi_i(x_{nk})\,\phi_j(x_{nk}) \tag{18}$$

$$D_{ij} = \int_0^L \rho A\,\phi_i\,\phi_j\mathrm{d}x + \sum_{n=1}^{N_m} m_n\,\phi_i(x_{nm})\,\phi_j(x_{nm}) \tag{19}$$

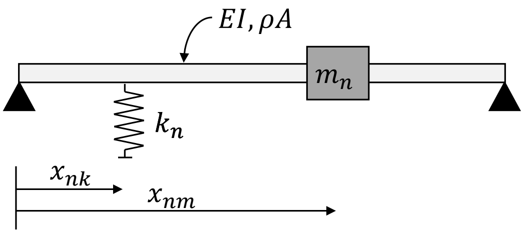

Fig. 13 Base with n'th spring and point mass.

The Rayleigh-Ritz method results in the eigenvalue problem in Eq. (20) where Λ is the eigenfrequencies.

$$\det\left(a_{ij} - \Lambda^2\,D_{ij}\right) = 0 \tag{20}$$

The mode shape amplitudes C_j can be recovered using Eq. (21), when one of the amplitudes are set to unity.

$$\sum_{j=1}^{n}\left[a_{ij} - \Lambda^2 D_{ij}\right]C_j = 0 \qquad \text{for} \qquad i = 1, 2, ..., n \tag{21}$$

To solve Eq. (20), equations are formulated for ϕ_n. These equations are obtained from the fourth order differential equation of a beam in bending and by applying the boundary conditions of the given problem. To exemplify the method, a pinned-pinned B.C. is explained in the following. For other types of boundary conditions refer to page 726 in [3]. The differential equation is solved using the boundary conditions resulting in the frequency equation shown in Eq. (22) and the mode shape term shown in Eq. (23). The frequency equation has an infinite number of solutions and is solved for the first n results of β_n which is used to get ϕ_n.

$$\sin(\beta_n\,L) = 0 \tag{22}$$

$$\phi_n(x) = \sin(\beta_n\,x) \tag{23}$$

Once the eigenfrequencies are determined the constants C_j are recovered using Eq. (21) and finally the mode shape for each eigenfrequency are found by using Eq. (24).

$$w_n = \sum_{i=1}^{N} C_i\phi_i \tag{24}$$

The mode shapes in Eq. (24) are discretised resulting in a mode shape vector. Then the vector is normalised, the absolute value of each entry is calculated, and the vectors are stored in a matrix $f_i(x)$ consisting of i mode shapes. This procedure is implemented in the app for six different configurations, with respective frequency equations and mode shape terms. The six configurations are, pinned-pinned, free-free, fixed-fixed, fixed-free, fixed-pinned and pinned-free.

The app is developed only to calculate the bending mode shape based on the user's input of the following:

- Base thickness, height, and length.
- Boundary condition of base.
- Masses and location.
- Springs and location.
- Number of modes shape solutions.
- Number of mode shapes to optimize for.

7.2 Optimum location of Smart Device

Based on the user's input, the optimum location of the Smart Device is determined using the weighted global criterion method in Eq. (25) where f_i^o is the utopia point located at $(1, 1, ..., 1)$ and Y_i is the weight factor. The weight factor is set to one but can in principle be set to any value to bias one mode shape over another. The exponent p is set to 2 to give the compromise solution of the problem where $D(x)$ is a vector of the Euclidean distances from the utopia point.

$$D(x) = \left(\sum_{i=1}^{N} Y_i\left(f_i(x) - f_i^o\right)^p\right)^{1/p} \tag{25}$$

The vector $D(x)$ is sorted from the lowest value to the highest and the entrance of the lowest value is saved. The entrance in the vector is related to the distance x resulting in the location for the Smart Device that maximises the stiffness of the system and thus changes the mode shapes the most.

To find a solution for the eigenfrequencies and mode shapes after the Smart Device is activated, the device and the optimum location are included as a spring in Eq. (18) and the entire procedure described in Section 7.1 is performed again.

The first three eigenfrequencies for a pinned-pinned B.C and the eigenfrequencies after the Smart Device is applied are shown in Tab. VI.

M.S.	Colour	$\Lambda_{i,off}$ [Hz]	$\Lambda_{i,on}$ [Hz]	Rel. increase [%]
1	Blue	25.3	71.5	183
2	Red	101	227	125
3	Yellow	227	343	51

Tab. VI Change in eigenfrequency from activation of Smart Device shown in Fig. 14.

The mode shapes before and after the Smart Device is activated are shown in Fig. 14 where the optimum location is found as $x \approx 0.4\,\mathrm{m}$ and $x \approx 0.8\,\mathrm{m}$ when including the two first mode shapes in the optimisation scheme. Two equally valid compromise solutions are found due to symmetry in the mode shapes.

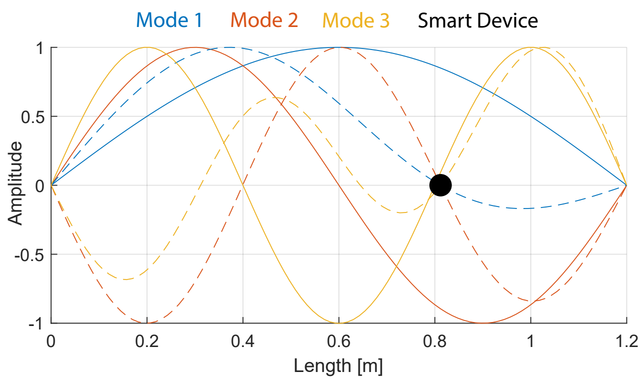

Fig. 14 Mode shapes before (full line) and after (dashed line) Smart Device (black point) is placed at $0.8\,\mathrm{m}$.

8. Conclusion

A device for semi-active vibration control of commercial skid pump systems has been developed throughout this project. The control strategy is adding or withdrawing stiffness from the system which result in a change in eigenfrequency. This is accomplished by clamping or releasing a shaft using friction to create an additional support. The final design is based on the results obtained from the explicit optimisation approach with adjustments to the geometry based on experience from the finite element simulations. Two different skid systems were investigated. For skid system I an increase of at least 131% of the original eigenfrequency is found from activating the Smart Device in the desired frequency range of $25\,\mathrm{Hz}$ to $100\,\mathrm{Hz}$. For skid system II limited effects of activating the Smart Device is observed with only 4% increase in the third eigenfrequency. To reduce vibrations on skid systems with legs of high stiffness like system II, another approach must be taken to the mounting of the Smart Device. The location of the Smart Device on must not be at nodal points of the relevant mode shapes as no change in eigenfrequency will be obtained. Similarly, care must be taken in determining the location, if a shifted eigenfrequency of one mode coincide with the original eigenfrequency of another mode. The performance of the final design is satisfactory based on simulations compared to the requirements. The height requirement is not fulfilled and further investigation is necessary to determine the consequence of this. Testing on a physical system is also necessary to demonstrate the performance in real life applications.

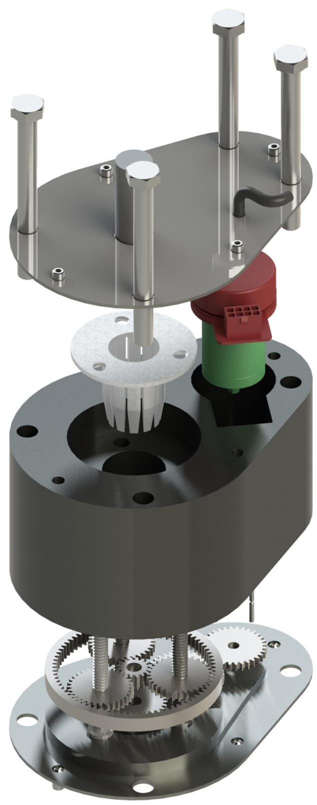

Fig. 15 Exploded view of final design.

Acknowledgement

The authors of this work gratefully acknowledge Grundfos for sponsoring the 10th MechMan symposium.

References

[1] A. C. Ugural, *Mechanical Design of Machine Components*. CRC Press, 2 ed., 2015.

[2] R. L. Norton, *Machine Design An integrated approach*. Worcester, Massachusetts: Prentice Hall, 5 ed., 2014.

[3] S. S. Rao, *Mechanical Vibrations*. Pearson, 5 ed., 2004.